Chapter 4

Gold nanoflower decorated $MoSe_2$ modified electrode for the electrochemical detection of free cholesterol

4.1 Introduction

Cholesterol is an important structural component of animal cell membranes and also constitutes several essential components of living organisms like steroid hormones, vitamin D, bile acids, etc. The sedentary lifestyle of humans with a lack of physical exercise and nutritional deficiency brings about the elevation of cholesterol levels in the blood [Kim et al., 2021; Ayilliath et al., 2021; Li et al., 2019]. The desirable concentration of cholesterol in the blood is below 5.2 mM (200 mg/dl), but an imbalance in the cholesterol level, i.e. > 6.2 mM (240 mg/dL) may lead to several fatal diseases like atherosclerosis hypertension, strokes, chronic kidney disease, type-2 diabetes, and neurological disorders such as Alzheimer's and Niemann-Pick disease. On the contrary, the lower levels may lead to anemia and hepatopathy [Ayilliath et al., 2021; Haritha et al., 2022]. To overcome such complications, it is crucial to develop a practical sensor that can aid in the accurate and regular monitoring of cholesterol levels. To date, various conventional techniques have been developed to quantify cholesterol, such as high-performance liquid chromatography [Usui et al., 2002], thin-layer chromatography [John et al., 2015], fluorimetry [Mondal et al., 2012], colorimetry [Nirala et al., 2018], etc. Although these techniques are accurate, they bear some limitations like labor-intensive, poor specificity, expensiveness, and time-consuming rendering them from real applications. Electrochemical biosensors present them as an alternative to conventional techniques because of their excellent sensitivity and selectivity with the potential to be transformed into portable devices [Yadav et al., 2021]. Differential Pulse Voltammetry (DPV) attracts significant interest since it can be used to elucidate the redox electrode process and estimate trace level amounts of

electroactive analytes [Mall et al., 2022]. Electrochemical Impedance Spectroscopy (EIS) technique provides label-free detection of the analyte, which involves the study of variation of interfacial charge transfer resistance (R_{ct}) and capacitance of the working electrode [Ojha et al., 2022]. These variations can be related to the enzymatic reaction for different substrate concentrations at the interface of biosensor electrodes and enable their quantification without any assistance of labels or markers. The cholesterol oxidase (ChOx) enzyme-based sensor bears good selectivity and sensitivity. ChOx acts as a crucial bioreceptor that catalyzes the oxidation of the cholesterol to cholestene-3-one and H_2O_2 as shown in the scheme below [Amiri et al., 2020; Bogomolova et al., 2009; Xu et al. 2019; Garrote et al., 2019].

$$\text{Cholesterol} \xrightarrow{\text{ChOx}} \text{Cholestene-3-one} + H_2O_2 \quad \text{....Eq 4.1}$$

The measurement of H_2O_2 generated gives an indirect assessment of the cholesterol concentration. However, such methods are sensitive to several interferences like ascorbic acid and uric acid as they are required to be carried out at high anodic potential. This problem was resolved by using a redox mediator, $[Fe(CN)_6]^{3-/4-}$ and recording the signal of it in place of H_2O_2 [Dijksma et al., 2002; Lazar et al., 2016]. With the development of nanotechnology, the rapid progress in the field of the development of electrochemical biosensors has been addressed with greater selectivity and sensitivity [Molecules, 2020]. Several nanomaterials based on noble metals like gold nanoparticles (AuNPs) [Aravind et al., 2011], Palladium nanoparticles (PdNPs) [Dong et al., 1993], Pd-Pt bimetallic [Cao et al., 2013], metal oxides like ZnO [Solanki et al., 2009], Fe_3O_4 [Kaushik et al., 2010], SnO [Ansari et al. 2009], carbon nanostructures [Gopalan et al., 2009; Ji et al., 2015], and polymers [Soylemez et al., 2015] have been reported for the detection of cholesterol. Recently, two-dimensional (TMDs) based nanomaterials such as graphene and its analogs like transitional metal

dichalcogenides have demonstrated their excellent catalytic efficiency and long-term stability, which has widened their scope in electronic to biomedical applications [Bolotsky et al., 2019]. Among all the layered materials, $MoSe_2$ is considered analogous to MoS_2 and shows greater potential in the same field of applications. Essentially, the conductivity of the $MoSe_2$ is comparably higher than MoS_2 due to the intrinsic metallic nature of Se (5×10^{-28} Sm^{-1} for S and 1×10^{-3} Sm^{-1} for Se). Further, as per the reports, the incorporation of the gold nanoparticles into $MoSe_2$ enhances its electrical and optical performances considerably [Wu et al., 2020; Eftekhari et al., 2017].

In this work, $MoSe_2$ nanosheets have been synthesized through a solvothermal technique. Further, gold nanoflower was grown onto the surface of $MoSe_2$ modified glassy carbon electrode (GCE), employing the reducing nature of synthesized nanosheets dipped in the gold salt solution. Au-$MoSe_2$ improves effective conductivity and redox properties with comparatively higher peak current and reduced peak separation. Cholesterol oxidase was immobilized onto $AuMoSe_2$ modified GCE surface and employed as a sensing probe for the detection of cholesterol through EIS and DPV techniques. The corresponding changes in charge transfer resistance (R_{ct}) and current due to the reaction of cholesterol oxidase enzyme with cholesterol were studied using $[Fe(CN)_6]^{3-/4-}$ as a redox mediator both in human serum and PBS buffer. The fabricated biosensor shows an improved electrochemical response for the sensing of cholesterol over a wide range of concentrations from 60 μM to 10 mM and a detection limit of 3.2 μM in DPV and 37 μM in the EIS technique, respectively.

4.2 Experimental

4.2.1 Chemicals

Glucose, Cholesterol oxidase, potassium ferrocyanide trihydrate ($K_4[Fe(CN)_6].3H_2O$), Cholesterol, Urea, L-Ascorbic acid, potassium ferricyanide ($K_3[Fe(CN)_6]$) were bought

from Merck. Sodium molybdate ($Na_2MoO_4.2H_2O$) and Selenium powder were purchased from Sisco Research Laboratories. Potassium dihydrogen phosphate (KH_2PO_4), Auric chloride ($HAuCl_4$), and dipotassium hydrogen orthophosphate (K_2HPO_4) are bought from Merck for the buffer preparation. Human blood serum was obtained from the laboratory of Prof. D. Das, Institute of Medical Sciences (IMS), Banaras Hindu University.

4.2.2 Instrumentation

Rigaku miniflex 600 X-ray diffractometer with Ni-filtered Cu Kα radiation (λ = 1.54056 Å) at a scan rate of 3º min^{-1} was used to get the XRD pattern. Scanning electron microscope [FE-SEM (Zeiss, Merlin)] at an accelerating potential of 20 V to 30 kV was used to study the surface morphology, and [FEI Tecnai-G2] transmission electron microscopy (TEM) was utilized to get information about the structural morphology of the samples. The material's chemical composition was studied by a Thermo scientific K-alpha X-ray photoelectron spectrometer. Electrochemical measurements (electrochemical impedance and cyclic voltammetry study) by using a standard three-electrode setup at room temperature (25 ºC) on Potentiostat/Galvanostat (Autolab (PGSTAT-302, The Netherlands)). A glassy carbon electrode (GCE) or modified GCE was utilized as the working electrode with a geometric area = 0.07 cm^2, platinum wire as the counter electrode, and a reference electrode of Ag/AgCl (saturated with KCl) was used. GC electrode surfaces were cleaned using a polishing pad mechanically with neutral alumina powder (0.05 µm) and rinsed with triply distilled water thoroughly, followed by ultrasonication for 10 min. Before measurements, high-purity N_2 purging was done in electrolytes for 20-25 minutes. The standard cholesterol solution was prepared by gently heating it at 60 ºC in the mixture of solvents of 2 mL Triton X 100, 7 mL phosphate buffer (pH 7.4), and 1 mL ethanol till a clear solution was obtained.

4.2.3 Synthesis of $MoSe_2$

$MoSe_2$ were synthesized through one-step solvothermal route (see Figure 4.1) using sodium molybdate ($Na_2MoO_4.2H_2O$) (24.2 mg) solution in ethanol-water mixture (10 mL; 1:1 v/v) and selenium powder (15.8 mg) in 10 mL ethylene diamine as precursors. The above solutions were mixed at room temperature (RT) stirring for 1 hour, and the pH was 12. The solution was then poured into the stainless steel-lined Teflon autoclave and left to proceed for three days, maintained at ~200°C. Further, the reaction mixture was brought to RT naturally, and the product was centrifuged at 6000 rpm. The precipitate was thoroughly washed with water followed by ethanol and dried at 70 °C.

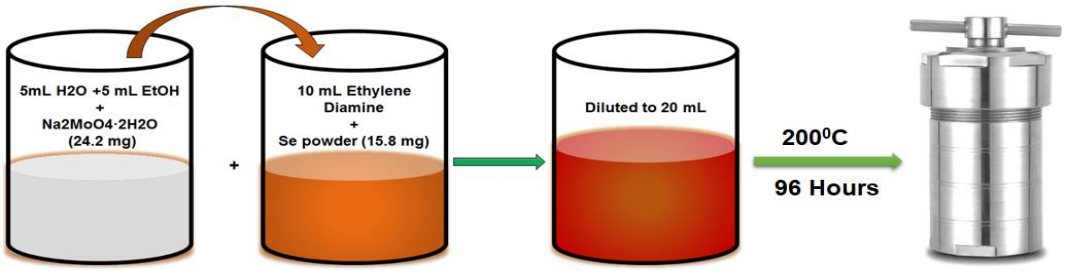

Figure 4.1 Scheme for the solvothermal synthesis of $MoSe_2$.

4.2.4 Growth of the gold onto $MoSe_2$

The synthesized $MoSe_2$ has intrinsic reducing properties which were utilized for the in situ growth of the gold on its surface. In the procedure, GC electrode surfaces were cleaned with alumina powder using a polishing pad and rinsed with triply distilled water thoroughly, followed by ultra-sonication for 10 min. Further, 10 μL of $MoSe_2$ suspension in water (1 mg/mL) was drop cast onto the glassy carbon electrode (GCE) surface and dried in a vacuum desiccator. The modified electrode was further dipped in 1 mM $HAuCl_4$ and incubated at room temperature for 30 minutes, as shown in Figure 4.2. During this period, the Au^{3+} ion gets reduced to Au^0 at the surface of the $MoSe_2$

nanosheet and facilitates the growth of gold nano-flower as evidenced by the SEM images.

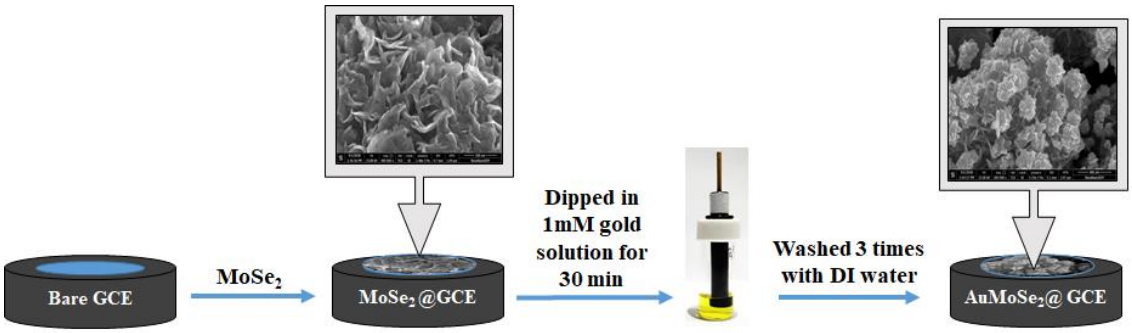

Figure 4.2 Schematic for the growth of gold nanoflower onto $MoSe_2$ modified GC electrode surface.

4.2.5 Electrode Modification Procedure

After modifying the GCE with $AuMoSe_2$ as described in Figure 4.2, the electrode was washed three times with triple distilled water followed by 0.1M PBS buffer (pH= 7.4). For the immobilization of the enzyme, 10 μL of ChOx, (10μg/mL) was drop casted, and the electrode was kept for incubation in a moisture chamber for 6 hours at room temperature. After incubation, the modified electrode was further washed three times with a PBS buffer to wash out the unbound enzymes. In the last, the nonspecific sites were blocked using 1% BSA by incubating the electrode for 1 hour. The electrode was finally washed three times with PBS buffer before performing the electrochemical measurements. All steps are identical for studying the human serum except BSA modification as serum itself blocks nonspecific sites. A schematic presentation for electrode modification is given in Figure 4.3.

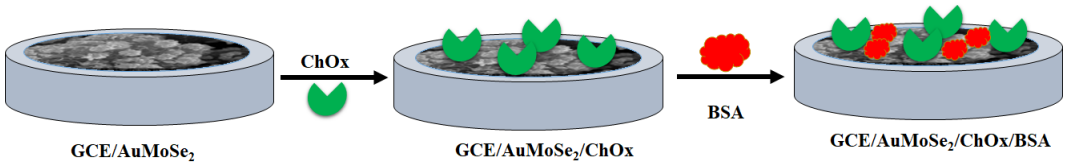

Figure 4.3 Schematic for the stepwise electrode surface modification of cholesterol biosensor.

4.3 Results and discussion

4.3.1 Materials Characterizations

The structural investigation of the synthesized $MoSe_2$ has been done using the X-ray diffraction (XRD) technique. Figure 4.4 (a) shows the XRD pattern of $MoSe_2$ having four distinct signature peaks at 8.4°, 33.2°, 41.6°, and 54.7° corresponding to (002), (100), (103), and (110) lattice planes. The obtained peaks are consistent with previously reported works following a standard pattern (JCPDS: 29-0914).[31] The result suggests that the synthesized $MoSe_2$ adopts a hexagonal crystal phase (2H-$MoSe_2$). (002) plane at a lower diffraction angle as compared to other reports [Balasingam et al., 2015] suggests the formation of more exfoliated nanosheets in as-synthesized $MoSe_2$.

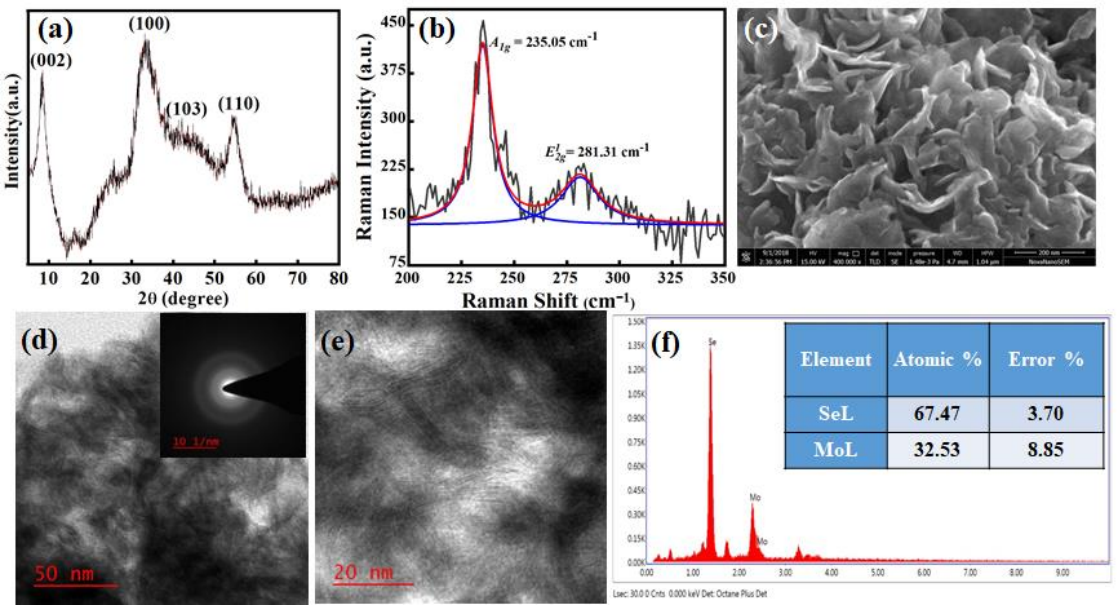

Figure 4.4 XRD spectra of $MoSe_2$ (a), Raman Spectra (b) and SEM image at 200 nm scale (c), TEM image at 50 nm scale (d), at 20 nm scale (e), EDS spectrum, SAED pattern (inset (d)).

The structural study of as-synthesized $MoSe_2$ nanosheets was done by using Raman Spectroscopy. The typical peaks at 235.05 cm^{-1} and 281.31 cm^{-1} of $MoSe_2$ nanosheets are observed in the Raman spectra (Figure 4.4b), which can be designated as out-of-plane A_{1g} mode and in-plane $E_{2g}{}^1$ mode, respectively [Sekine et al., 2013]. In the case of bulk $MoSe_2$, the A_{1g} mode is observed at 242 cm^{-1}. The downward shift of ~7 cm^{-1} (A_{1g} mode @ 235.05 cm^{-1}) stipulates the formation of few-layered $MoSe_2$ nanosheets [Balasingam et al., 2015]. The morphological study of $MoSe_2$ was done using scanning electron microscopy (SEM), as shown in Figure 4.4c. From the SEM image, we can observe that as-synthesized $MoSe_2$ has a layered structure stacked together in a flower-like morphology. As shown in Figures 4.4 d & e, the TEM images show that a typical layered nanosheet structure is clearly visible in the as-synthesized $MoSe_2$. The image at a higher magnification reveals some lattice fringes having periodic contrast modulation with a period of 0.66 nm. This length was found to be comparable with our XRD findings of the interplanar distance along (00*l*) in the 2H-$MoSe_2$ [Balasingam et al., 2015; Li et al., 2019]. The Inset of Fig 4.4 d shows the Selected Area Electron Diffraction (SAED) Patten which is recorded in the same region as shown in the TEM images. The SAED pattern is found to be a diffused ring pattern, as expected from the solvothermally synthesized $MoSe_2$. The elemental composition of the $MoSe_2$ has been further investigated using Energy-dispersive X-ray spectroscopy (EDS). Figure 4.4 (f) shows the EDS spectrum of the $MoSe_2$, evidencing the presence of elements Mo and Se. The calculated atomic percentage of Mo and Se is found to be in a ratio of 1: 2.07, which is close to its stoichiometric ratio.

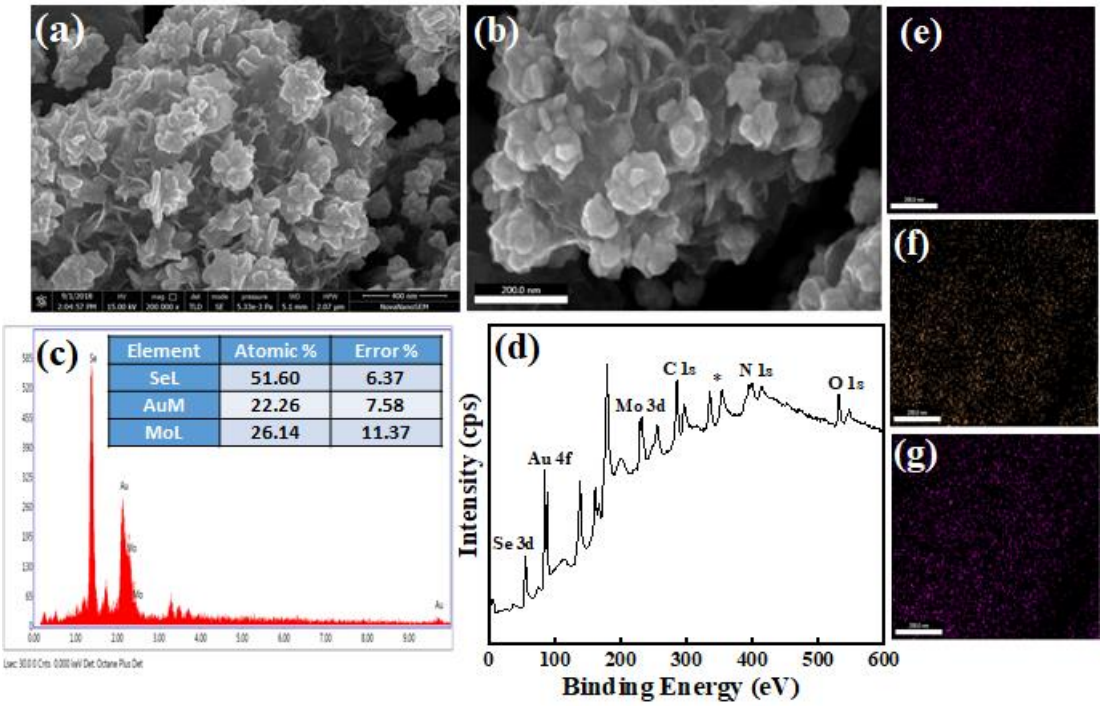

Figure 4.5 $AuMoSe_2$ Characterization (a) SEM image at 400 nm scale, (b) at 200 nm scale for mapping, (c) EDS spectrum, (d) XPS survey (e) Elemental mapping image for Mo, (f) Au, (g) Se.

After confirming the formation of a pure phase $MoSe_2$ nanosheet, the synthesized $AuMoSe_2$ has also been studied through multiple characterization techniques like SEM, EDS, XPS, and EDS mapping. Figure 4.5 a & b show the SEM images of gold decorated $MoSe_2$. As can be seen from the images, the nanosized flower-like morphology of Au has grown onto the surface of the nanosheet. EDS spectrum was recorded to confirm the elemental composition of $AuMoSe_2$. The presence of Au element along with Mo and Se clearly exemplified the growth of the gold on $MoSe_2$ as shown in Figure 4.5 c. Further, the detailed elemental composition was also inspected from XPS, as shown in the XPS survey Figure 4.5 d, the presence of Au in a reduced state validates the successful decoration of gold on the $MoSe_2$ surface. The distribution of the elements was also inspected using EDS mapping, as shown in Figure 4.5 e-g. The area used for the EDS mapping corresponds to the SEM image shown in Figure 4.5 b. It can be seen that uniform distribution of Mo and Se is observed while the distribution of

the Au in the image is concentrated around the nanoflower-like structures grown on $MoSe_2$ nanosheets. The detailed analysis of the XPS spectrum was done using the deconvoluted spectrum of the XPS. As can be observed in Figure 4.6 a, there are four deconvoluted peaks for Mo 3d level. The two peaks at 231.8 and 234.9 eV can be assigned to $3d_{5/2}$ and $3d_{3/2,}$ respectively, for Mo in a +5 oxidation state. The other two peaks at 232.4 and 235.4 eV are attributed to $3d_{5/2}$ and $3d_{3/2,}$ respectively, for Mo in a +6 oxidation state [Castillo et al., 2016; Wei et al., 1998; Choi et al., 1996]. The oxidation of Mo from Mo^{4+} to Mo^{5+}/Mo^{6+} may be due to the reduction of the Au^{3+} during gold decoration. Figure 4.6 b illustrates three deconvoluted XPS peaks for the selenium 3d level. The peaks at 54.1 eV and 56.1 eV can be attributed to $3d_{5/2}$ and $3d_{3/2,}$ respectively, which is consistent with the pristine $MoSe_2$ with a little change in $3d_{3/2}$ binding energy as shown in Figure 4.6 e, while a distinctive peak was observed at 58.5 eV in the $AuMoSe_2$ assigned to SeO_x doublets, which is probably due to the oxidation of $MoSe_2$ by $HAuCl_4$ to form gold nanoflower [Zhao et al., 2017; Xiao et al., 2017]. Figure 4.6 c shows the Au 4f doublets at 83.6eV and 87.2eV corresponding to $4f_{7/2}$ and $4f_{5/2}$ respectively. The observed peaks correspond to the zero oxidation state of Au, suggesting the reduction of $HAuCl_4$ at its surface [Xiao et al., 2017]. The deconvoluted peaks corresponding to Mo and Se of pristine $MoSe_2$ are shown in Figures 4.6 d and e respectively.

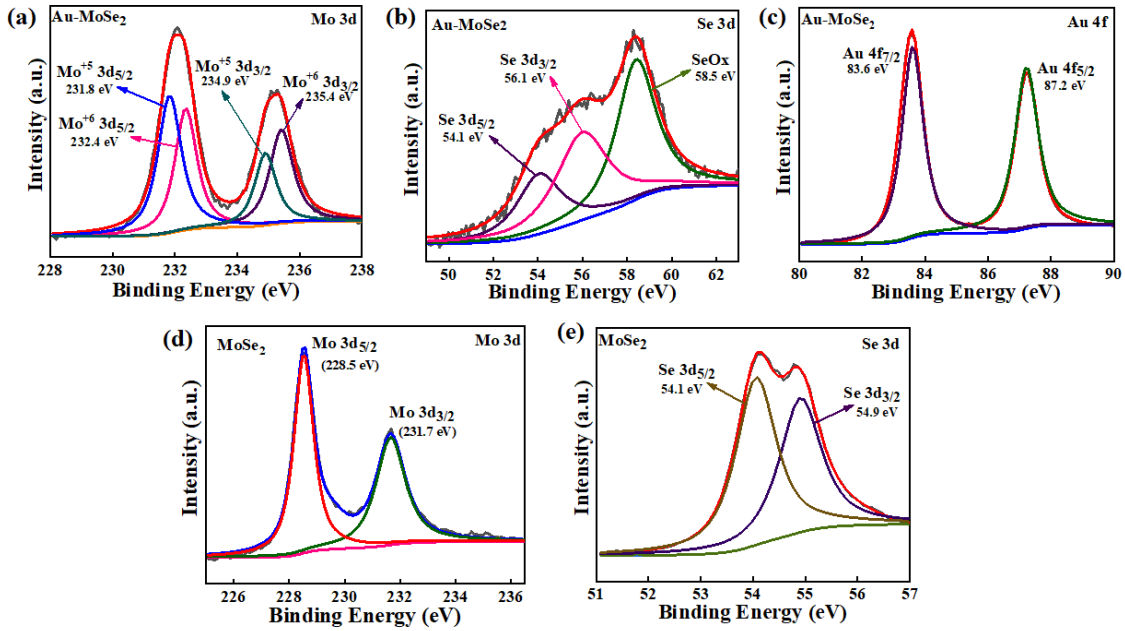

Figure 4.6 High resolution deconvoluted spectra of (a) Mo 3d, (b) Se 3d, (c) Au 4f for Au-$MoSe_2$ and (d) Mo3d, Se 3d for pristine $MoSe_2$.

4.3.2. Electrochemical characterization of the modified GCE

During the fabrication of the biosensor electrode, each step of probe preparation was monitored using cyclic voltammograms and EIS measurement in electrolyte using 5.0 mM $[Fe(CN)_6]^{3-/4-}$ in 0.1M PBS buffer (pH 7.4). Figure 4.7a shows the cyclic voltammograms of GC, GC/g-$MoSe_2$, GC/Au$MoSe_2$ and GC/Au$MoSe_2$/ChOx/BSA. In the graph, we can compare the peak current and peak separation of GC/$MoSe_2$ and GC/Au$MoSe_2$, the peak separation in the case of GC/Au$MoSe_2$ was found to be comparatively reduced with the significantly enhanced current. The result suggests synergistic enhancement of the electrochemical properties of $MoSe_2$ upon decoration by the gold nanoflower. The stepwise modification of the surface of the biosensor was monitored through CV and EIS techniques. The CVs were recorded in the potential range of -0.2 to 0.6 V at the scan rate of 10 mV/s and EIS measurement was done at open circuit potential in the frequency range of 0.1Hz to 100 kHz with an amplitude of 0.01V as shown in Figure 4.7 b. From Figures 4.7 a & b, it can be concluded that after modification of the GC with Au$MoSe_2$, the current was increased, and relative charge

transfer resistance was decreased. Further, after modifying the probe with the enzyme ChOx, the interfacial charge transfer resistance is increased with the decreased current value. The result suggests the successful immobilization of the enzyme on the $AuMoSe_2$ surface. The decrease in current and enhanced charge transfer resistance is the consequence of the insulating nature of the enzyme.

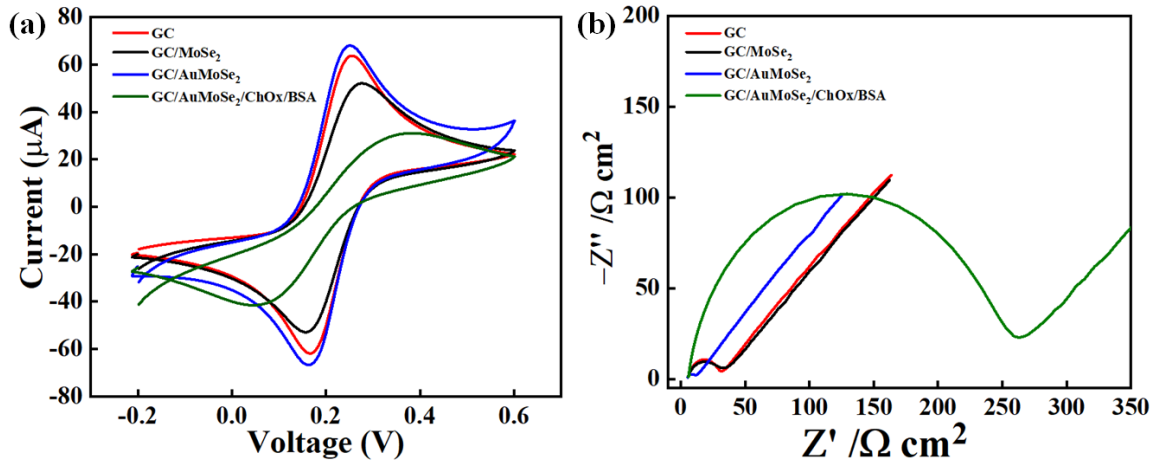

Figure 4.7 (a) CV of surface modified GC for bare GC, GC modified with $MoSe_2$, $AuMoSe_2$, and $AuMoSe_2$/ChOx/BSA. (b) Nyquist plot of surface modified GC for bare GC, GC modified with $MoSe_2$, $AuMoSe_2$, and $AuMoSe_2$/ChOx/BSA.

4.3.3 Sensing of cholesterol

After the successful fabrication of the biosensor probe and its characterization, the response of the probe has been investigated with different concentrations of cholesterol in PBS buffer and human serum. As shown in Scheme 4.1, the cholesterol in the presence of enzyme ChOx gets oxidized to cholest-4ene-3one and generates H_2O_2. These get further reduced and generates electron to the modified electrode surface to give respective current or impedance change. The response of the probe was measured as the function of change in current in DPV and charge transfer resistance (R_{ct}) in the EIS technique. In PBS buffer, as shown in Figures 4.8 a & b, there is a decrease in current in the DPV technique and enhancement in the charge transfer resistance in the EIS technique, respectively, with increased cholesterol concentration. The above

observations are in contrast to the reports, where an increase in the current is observed with an increase in cholesterol concentration [Gopalan et al., 2009].

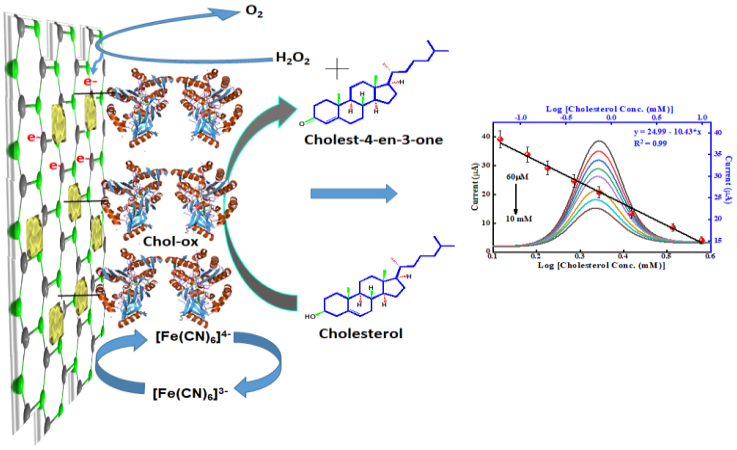

Scheme 4.1 Schematic for cholesterol sensing.

As per the report published by Vidal (1999) [Vidal et al., 1999] and M. Alagappan (2020) [Alagappan et al., 2020], there is a trade-off in the current observed, dependent on cholesterol and surfactant. There is an increase in current with cholesterol addition but simultaneously decrease in current occurs due to Triton-X 100 concentration present in cholesterol. Thus the concentration of the Triton-X 100 becomes crucial in guiding the analytical response. The Nyquist plot related to each addition of cholesterol in PBS was fitted with the most appropriate equivalent circuit (inset of Figure 4.8b). R_{ct} values were calculated from the EIS spectra using the equivalent circuit RQRW, as shown in the inset of Figure 4.8(b). The change in interfacial charge transfer resistance (ΔR_{ct}) was plotted with the cholesterol concentration. The ΔR_{ct} was calculated by using the equation.

$$\Delta R_{ct} = R_{ct \text{ of the probe after addition of cholesterol}} - R_{ct \text{ of the probe before cholesterol addition (blank)}} \quad \text{(Eq 4.2)}$$

In PBS, the biosensor shows a linear response from 60 mM to 10 mM following linear regression equation ΔR_{ct} = 24.99 – 10.43*log [Cholesterol Conc./(mM)], R^2 = 0.99 in

case of DPV technique, whereas in EIS technique, it follows the linear equation ΔR_{ct} = 82.67 + 39.83 log [Cholesterol Conc./(mM)] R^2 = 0.98. The limit of detection (LOD) for the constructed biosensor was found to be 3.2 and 37 µM in DPV and EIS techniques, respectively (LOD = $3S_b/m$, where S_b stands for the standard deviation of the blank signal and m stands for the slope of the linear portion of the calibration plot).

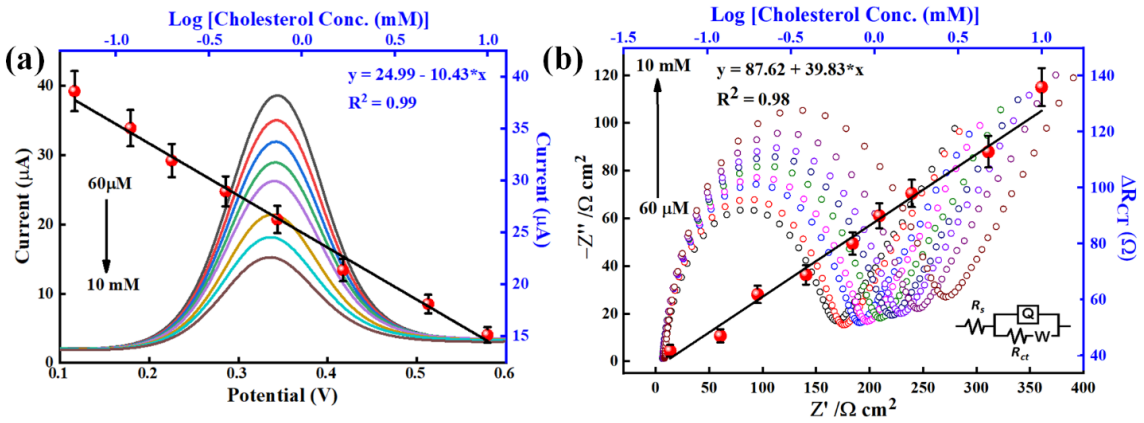

Figure 4.8 (a) DPV, and (b) Nyquist plot for GC/Au-$MoSe_2$/Chol-Ox-BSA in PBS (60 µM to 10 mM) with corresponding calibration plots in 0.1M PBS buffer (pH= 7.4) containing 5mM $[Fe(CN)_6]^{3-/4-}$. The inset of Figure 4.8b shows the most compatible equivalent circuit.

4.3.4. Interference study

The developed biosensor has been tested for its selectivity towards cholesterol. The study checked the electrochemical response and its cross-reactivity with several possible biological interferences like glucose, ascorbic acid, urea, and BSA. The bar graph shown in Figure 4.9 reveals the response of the fabricated cholesterol biosensor with ten times greater concentrations of various biological interferences (10 mM) and cholesterol (1mM). As can be concluded from Figure 4.9, there are insignificant changes in the response of the developed biosensor even though the concentration of the interferences is ten times that of the cholesterol. The result suggests good selectivity of the developed biosensor, making it effective for application in real sample analysis.

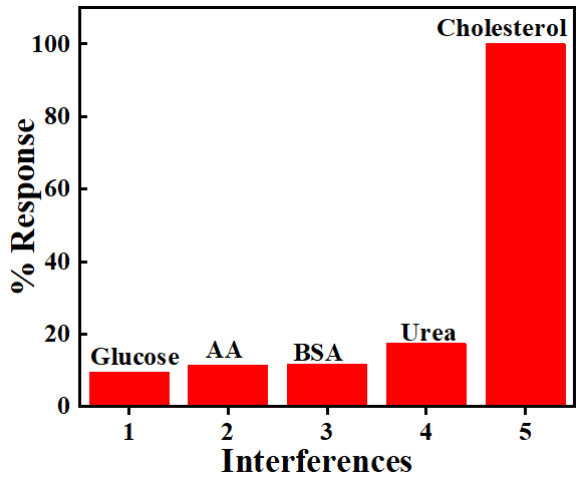

Figure 4.9 Interference study for the selectivity of cholesterol biosensor with various biological analytes. The interfering analytes concentration was 10 mM, and it was 1 mM for cholesterol.

Further, the sensor performance was investigated in human blood serum. For the study, the human blood serum was diluted ten-fold and spiked with different cholesterol concentrations. Figure 4.10 a & b show the DPV response curve and Nyquist plot for different cholesterol concentrations spiked in human (male) serum. the biosensor shows a linear response from 120 μM to 7.5 mM following linear regression equation ΔR_{ct} = 21.16 – 6.98*log [Cholesterol Conc./(mM)], R^2 = 0.98 with detection limit of 22 μM in case of DPV technique, whereas in EIS technique, a linear response from 60 μM to 10 mM is obtained with the linear equation ΔR_{ct} = 55.77 + 40.78*log [Cholesterol Conc./(mM)] R^2 = 0.99 and 60μM detection limit. The obtained trends were similar to that of PBS buffer but with reduced slope and linear range, which may be due to the complex matrix effect of the blood serum.

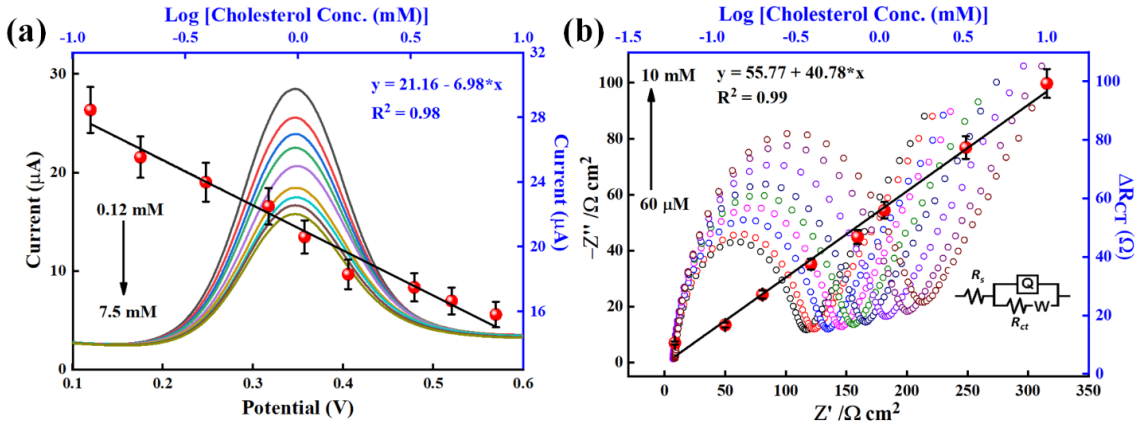

Figure 4.10 (a) DPV, and (b) Nyquist plot for GCE/AuMoSe$_2$/ChOx in human serum with corresponding calibration plots in 0.1M PBS buffer (pH= 7.4) containing 5 mM $[Fe(CN)_6]^{3-/4-}$. The inset of Figure 4.10 b shows the most compatible equivalent circuit.

The LOD of the developed biosensor was calculated and found to be lower or comparable to the previous reports of cholesterol biosensors, as shown in Table 4.2. In the view of real-time application, the developed biosensor has been investigated for its performance in real samples. In the study, the ten times diluted human blood serum was spiked with three known concentrations (0.12, 1.0, 3.3mM), and the percentage recovery was calculated from the calibration plot. The obtained recovery corresponding to the spiked concentrations is listed in Table 4.1. The result suggests a good recovery of the sample with better accuracy. Further, the sensitivity and accuracy of the comparison of the developed sensor are done with previously reported works on the ground of linear range and LOD, as given in Table 4.2. As can be assured that the proposed sensors have better LOD and are functional over a wide linear range of cholesterol concentration.

Table 4.1 Recovery data for the developed biosensor spiked with a known amount of cholesterol in human serum

S. No.	Amount of Cholesterol added (mM)	Amount of Cholesterol found (mM)	Recovery %	Relative standard deviation (RSD)
1	0.12	0.11	92	2.2 %
2	1.00	1.00	100	4.2 %
3	3.30	3.40	103	3.3 %

Table 4.2. Comparison table of the analytical parameters for the proposed cholesterol biosensor with previously reported sensors.

Materials	Method	Linear range (μM)	LOD (μM)	Reference
ChEt-ChOx/ZnO-CuO/ITO/glass	CV	500.0–12 000.0	500.0	Batra et al., 2015
ChOx/ZnO(T)/CT/GCE	CV	400.0–4000.0	200.0	Giri et al., 2012
AuE/dithiol/AuNPs/MUA/ChOx	CV	40.0–220.0	34.6	Saxena et al., 2010
Pt-PANI/Polyimide	Amperometry	1000–12,000	440	Gao et al., 2019
NiO/Si	Amperometry	120–10,230	100	Kaur et al., 2018
Pt/rGO/PABA SPCE	Amperometry	250–400	40.5	Phetsang et al., 2019
Si-GO-g-CMNC	DPV	647.5–10360	98.6	Anirudhan et al., 2018
Au-$MoSe_2$	**DPV** **Impedimetry**	**60-10000** **60-10000**	**3.2** **37**	**This work**

In order to investigate the reproducibility of the fabricated cholesterol biosensor, the three modified electrodes were prepared in similar conditions and their response was tested with a 5mM concentration of cholesterol. The result (as shown in Figure 4.11 a) clearly suggests that the electrodes have a similar response with a little deviation of around 5%. Further, the stability of the biosensor was also investigated by recording the response for 5 hours over an interval of 1 hour. As shown in Figure 4.11 b, there is a little alteration in response is observed. The results clearly suggest the highly reproducible and stable nature of the fabricated biosensor.

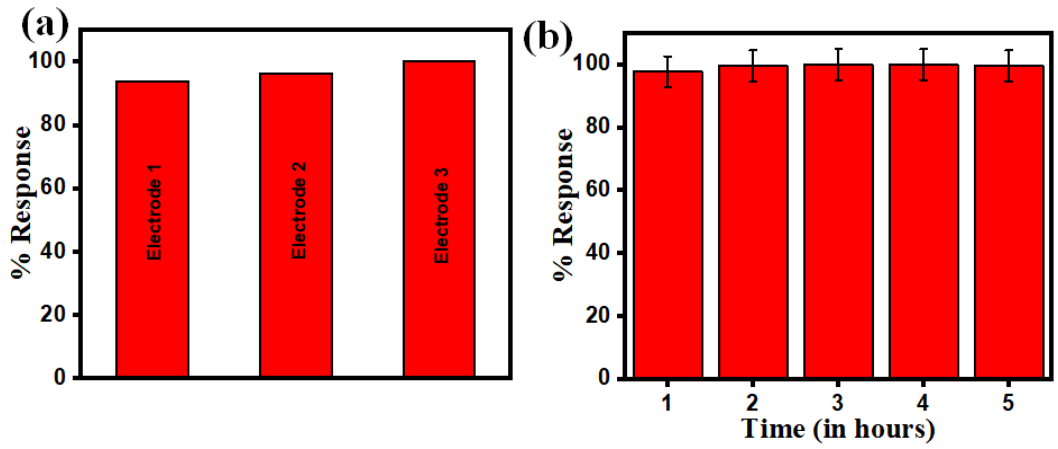

Figure 4.11 (a) The reproducibility study of five different biosensor electrodes with 5mM concentration of cholesterol (b) The stability study of the biosensor electrode over the period of 5 hours.

Further, the accuracy and sensitivity of the developed sensor have been compared with previously reported works on the ground of linear range and LOD, as shown in Table 4.2. It can be clearly seen that the proposed sensors have better LOD and are functional over a wide linear range of cholesterol concentration.

4.4. Conclusion

Herein, we have successfully synthesized and characterized the $MoSe_2$ nanosheet. Further, in situ surface modification of $MoSe_2$ with gold nanoflower was achieved at room temperature without any use of a reducing agent. The $AuMoSe_2$ shows excellent electrochemical properties and has been utilized to fabricate cholesterol biosensors by immobilizing ChOx. The developed biosensor has been used to detect cholesterol in PBS buffer and human serum with a limit of detection of 3.2 μM in DPV and 37 μM in EIS technique, respectively. The present study shows that the fabricated can be used as a potential electrochemical method for the point-of-care diagnosis of free cholesterol in real samples.